Dependence of excited-state properties of tellurium on dimensionality: From bulk to two dimensions to one dimensions

Yuanyuan Pan,[1,2] Shiyuan Gao,[2] Li Yang,[1,2,3,*] and Jing Lu[1,4,†]

[1]*State Key Laboratory of Artificial Microstructures and Mesoscopic Physics and Department of Physics, Peking University, Beijing 100871, People's Republic of China*

[2]*Department of Physics, Washington University in Saint Louis, Saint Louis, Missouri 63130, USA*

[3]*Institute of Materials Science and Engineering, Washington University in Saint Louis, Saint Louis, Missouri 63130, USA*

[4]*Collaborative Innovation Center of Quantum Matter, Beijing 100871, People's Republic of China*

(Received 24 February 2018; revised manuscript received 5 June 2018; published 22 August 2018)

The dependence of excited-state properties on dimensionality is the most prominent character of nanostructures. Using first-principles many-body perturbation theory, we show how those excited-state properties, i.e., quasiparticle energies and excitons, evolve with the dimensionality of tellurium nanostructures that have attracted significant interest because of their high carrier mobility and air stability. Even though the elementary atomistic structures are similar, dimensionality dictates many-electron interactions and excited-state properties: the self-energy correction to the band gap is increased from 0.22 eV in bulk to 0.90 eV in a two-dimensional (2D) monolayer, and ultimately to 2.70 eV in a one-dimensional (1D) spiral tube; excitonic effects are weak in bulk with an exciton binding energy less than 10 meV, while the exciton binding energy is substantially enhanced to be 0.67 eV in the monolayer and 2.40 eV in the 1D structure. Interestingly, reduced dimensionality also produces substantial anisotropic optical response through many-electron interactions: local-field effects dominate the optical spectra of 2D and 1D structures and induce highly anisotropic optical responses. These results not only reveal a systematic picture for understanding the evolution of excited-state properties with dimensionality but also suggest the possibility of designing macroscopic electronic and optical properties by engineering nanosized building blocks.

DOI: 10.1103/PhysRevB.98.085135

I. INTRODUCTION

Quasi-one-dimensional (1D) and quasi-two-dimensional (2D) crystals have attracted tremendous attention in recent years because of their novel properties and potential for broad applications in electronics, optoelectronics, and spintronics [1–6]. As the dimensionality is reduced from three-dimensional (3D) to 2D and 1D, Coulomb interactions between electrons are enhanced, dramatically enlarging many-electron effects and inducing novel excited-state properties. For example, the exciton binding energy is usually negligible (about a few meV) in bulk semiconductors, such as Si and GaAs, while it is about a few hundred or even thousands of meV in 1D and 2D semiconductors [7–12]. Despite many studies on individual nanostructures, a systematic understanding of how quantum confinement impacts excited-state properties and, particularly, how many-electron effects evolve with the dimensionality is still not complete. This may be because there are very few materials that can be constructed by using the same elementary building blocks to cover all of bulk, 2D, and 1D structures. For example, there are 1D carbon structures, such as carbon nanotubes (CNTs) [13] and graphene nanoribbons (GNRs). However, CNTs and GNRs do not naturally form 2D structures (graphene) and bulk (graphite). As a result, the electronic structures and excited-state properties among graphite, CNTs, and GNRs are impacted by not only the quantum confinement but also edge (passivation) and warping effects.

Bulk tellurium (Te) is a *p*-type semiconductor with an indirect band gap of ∼0.35 eV [14]. Particularly, a Te crystal is composed of individual helical Te chains stacked together and held by van der Waals (vdW) force. Thus, a Te crystal is also considered as a 1D vdW solid [15,16]. Recently, large-area solution-grown 2D tellurium (termed by tellurene) with a pronounced high carrier mobility and air stability has been successfully fabricated by a substrate-free solution phase process and mechanical exfoliation [17–20]. The experiment demonstrates that mechanical exfoliation has the potential to fabricate single-atom chains of Te [18]. Substantial quantum confinement effects have been observed in ultrathin 2D Te made of helical Te chains [19,21,22]. Therefore, the elementary helical Te chain structure serves as a natural and unique candidate for studying how the excited-state properties, i.e., the quasiparticle energies and excitons, evolve with the dimensionality of solids that have the same nanosized building blocks.

In this paper, we employ the first-principles GW-Bethe-Salpeter equation (BSE) simulation to explore the quasiparticle band energy and electron-hole (*e*-*h*) interactions of Te structures: bulk, 2D, and 1D. These many-electron effects are strongly influenced by the dimensionality: the self-energy correction of the band gap is increased from 0.14 eV in bulk Te to 0.9 eV in monolayer Te, and further to 2.7 eV in the 1D chain of Te. This dimensional effect is more significant in excitonic effects: the exciton binding energy is less than

*Corresponding author: lyang@physics.wustl.edu

†Corresponding author: jinglu@pku.edu.cn

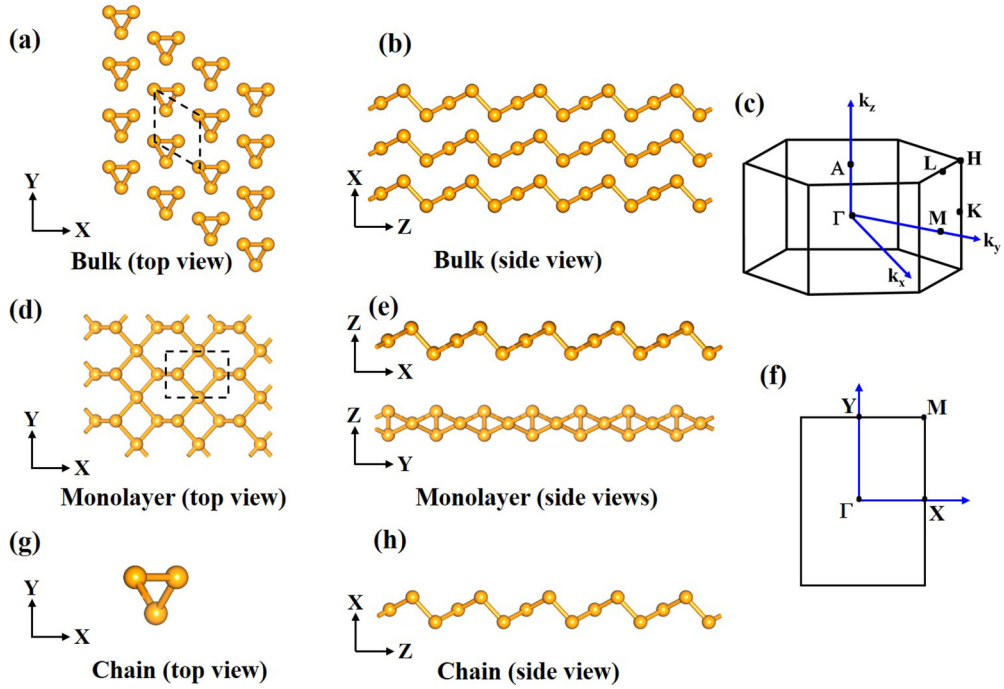

FIG. 1. (a–h) Top (left panel) and side (middle panel) view of bulk (a, b), monolayer (c, d), and chain (e, f) tellurium. (c–e) Brillouin zones of bulk (c) and monolayer (f) tellurium.

10 meV in bulk Te, while it is substantially increased to 0.67 eV in the monolayer and further to 2.40 eV in the 1D structure. In addition to impacting energies of quasiparticles and excitons, dimensionality also determines optical polarization properties through many-electron interactions and the depolarization effect. The 1D and 2D structures exhibit substantial anisotropic optical responses: they mainly absorb and emit light polarized along the chain direction or along the in-plane directions. However, the optical spectrum is nearly isotropic in the 3D structure.

II. COMPUTATIONAL METHODS

The structures are fully relaxed by density functional theory (DFT) with the general gradient approximation using the Perdew-Burke-Ernzerhof (PBE) [23] exchange-correlation potential implemented in the QUANTUM ESPRESSO package [24]. The ground state and eigenvalue are obtained with the norm-conserving pseudopotential [25]. The plane-wave basis is set with a cutoff energy of 60 Ry. A k-point sampling grid in the reciprocal space is $1 \times 1 \times 8$ for a chain of Te, $8 \times 11 \times 1$ for monolayer Te, and $12 \times 12 \times 8$ for bulk Te. The total energy is converged to be within 1×10^{-6} eV. There are three atoms per unit cell of all the structures. To avoid the interactions of periodic structures, for monolayer Te, a vacuum space of 15 Å is added along the direction perpendicular to the monolayer Te surface; for a chain of Te, a vacuum space of 15 Å is added along the two directions perpendicular to the chain direction.

The GW-BSE calculations are performed using the BERKELEYGW code [26] including the slab Coulomb truncation for monolayer Te and the wire truncation for a Te chain [27,28]. Quasiparticle band energy is calculated using the single-shot G_0W_0 approximation within the general Plasmon pole model [29]. The involved unoccupied conduction band number is about ten times the occupied valence band number for achieving the converged dielectric function and quasiparticle band gaps. The $1 \times 1 \times 12$, $12 \times 16 \times 1$, and $9 \times 9 \times 6$ coarse k grids are used in calculating GW quasiparticle band gaps and the coarse-grid e-h interaction kernels of bulk, monolayer, and spiral Te structures, respectively. In solving the BSE for the converged exciton energies and optical spectra, we use a fine k-point grid of $1 \times 1 \times 60$ for a chain of Te, $60 \times 80 \times 1$ for monolayer Te, and $36 \times 36 \times 24$ for bulk Te. At the GW-BSE level, following the previous work [30], we consider the first-order spin-orbit correction (SOC) by using the energy difference between the two Kohn-Sham split eigenvalues to correct the GW quasiparticle energies. On the other hand, the impact of SOC on the dielectric screening is not included in the GW-BSE calculations. Since SOC usually reduces the band gap, it will essentially increase the screening and thus reduce electron-electron and electron-hole interaction. As a result, the GW corrections and exciton binding energy may be slightly overestimated.

III. RESULTS AND DISCUSSIONS

A. Bulk Te

The structure of bulk Te is presented in Figs. 1(a) and 1(b). The most important character of this bulk structure is that it is constructed by bundles (arrays) of 1D spiral Te chains, which are stacked together by vdW force. Strong interchain coupling appears in monolayer Te as presented in Figs. 1(d) and 1(e), which is consistent with previous studies [20,21,31,32]. The first Brillouin zone (BZ) and high-symmetry points of bulk Te are plotted in Fig. 1(c). The DFT-calculated lattice constants of bulk Te are $a = b = 4.47$ Å and $c = 5.90$ Å, which are in a good agreement with available measurements, as shown in the

TABLE I. Lattice constant of bulk Te, monolayer Te, and chain Te.

	a (Å)	b (Å)	c (Å)
Bulk Te	4.47 (our result) 4.46 [33,34] 4.45 [20]	4.47 (our result) 4.46 [33,34] 4.45 [20]	5.90 (our result) 5.92 [34], 5.93 [33] 5.93 [20]
Monolayer Te	5.60 (our result) 5.49 [21,35,36]	4.20 (our result) 4.17 [21,35,36]	
Te Chain			5.66

Table I [20,33,34]. The lattice constants of monolayer Te are $a = 5.60$ Å and $b = 4.20$ Å, which are in a good agreement with the previous theoretical ones [21,35,36], and the lattice constant of chain Te is $c = 5.66$ Å.

The DFT-calculated band structure without SOC along the high-symmetry directions of bulk Te is shown in Fig. 2(a) (black lines). The conduction band minimum (CBM) is located at the H point, while the valance band maximum (VBM) is also around the H point but slightly away. Therefore, bulk Te is regarded as a nearly direct band-gap semiconductor. The DFT-calculated indirect band gap is about 0.17 eV and the direct band gap is about 0.19 eV at the H point. Importantly, the sharp band dispersion of the CBM results in a small effective mass of electrons, which contributes to the observed high electron mobility of bulk Te [37]. After considering the self-energy correction through the single-shot G_0W_0 approach (the blue line), the band gap is still nearly direct: the direct one is enlarged to be 0.41 eV and the indirect one is around 0.39 eV. Such a 116% enhancement (self-energy correction) of the quasiparticle band gap is similar to those of bulk semiconductors. For example, the band gap of bulk silicon is increased by the GW calculation to be 1.29 eV from the DFT value of 0.52 eV, which is also around 148% [29]. The DFT-calculated band structure of bulk Te after considering SOC is shown in Fig. 1(a) by the light-blue lines. SOC induces the splitting of the conduction band along the $\Gamma \rightarrow$A high-symmetry line, and bulk Te shows metallic bands with zero band gap. The DFT-calculated band gap with SOC around the H point is about 0.03 eV. For bulk Te, however, the band gap observed via the transmission spectra and photoconductivity spectra experiments is 0.32–0.33 eV. [38]. As listed in Table II, our GW-calculated quasiparticle band gap with SOC included is about 0.25 eV. This 70-meV discrepancy is already within the typical error bar of the single-shot G_0W_0 approach.

The optical absorption spectra of bulk Te are presented in Figs. 2(b) and 2(c). The optical absorption is defined as the imaginary part of the dielectric function [39]. Given the strongly anisotropic structure of bulk Te, we show the optical spectra for the incident light polarized perpendicular to the axial direction [the x/y direction in Fig. 1(a)] and along the axial direction of spiral Te [the z direction in Fig. 1(b)], which are shown in Figs. 2(b) and 2(c). First, let us focus on the

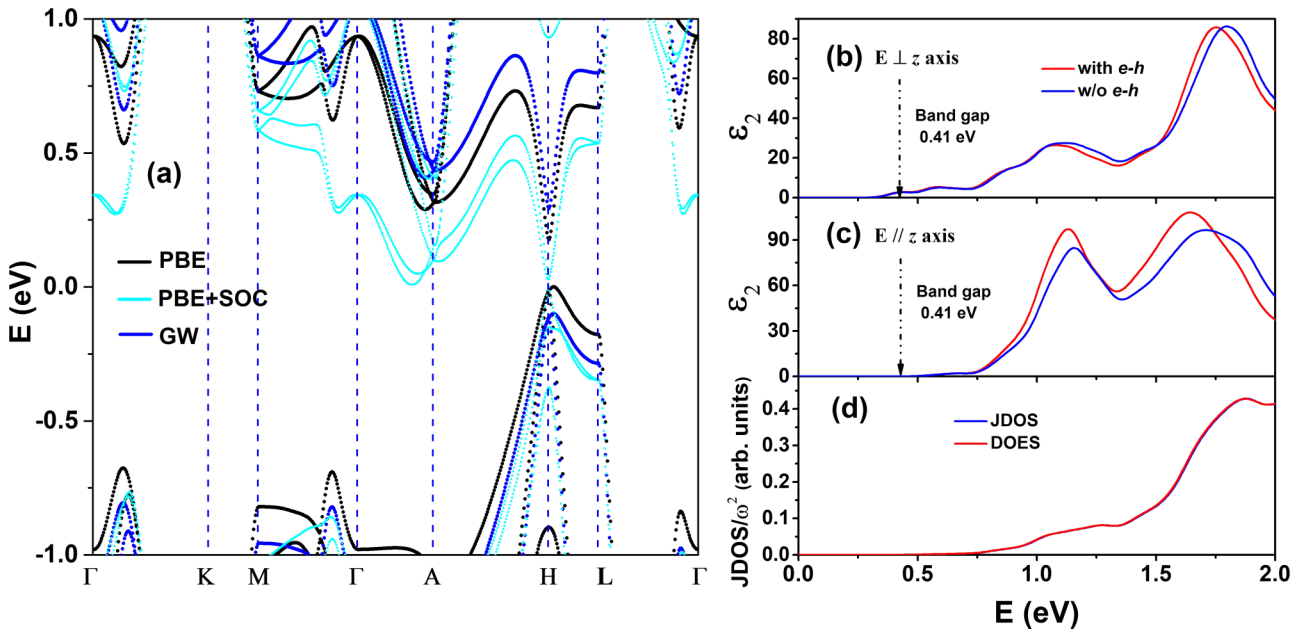

FIG. 2. (a) Band structure of bulk Te. The black, light blue, and blue line represent the band structures calculated at DFT-PBE, DFT-PBE-SOC, and GW level, respectively. (b, c) Optical absorption spectra (calculated without including SOC effects) of bulk Te for the incident light polarized along the x (b) and z (c) direction, respectively. The single-particle optical absorption spectra and those spectra with inclusion of e-h interaction are presented by the blue and the red solid line, respectively. (d) Interband joint density of states (JDOS) (blue line) and density of excitonic states (DOES) (red line). They nearly coincide.

TABLE II. Comparison of band gaps and exciton binding energies with the dimensionality. E_g^{PBE} and E_g^{GW} are the direct band gaps calculated by the DFT-PBE and GW methods, respectively. $E_g^{PBE+SOC}$(eV) and E_g^{GW+SOC}(eV) are the direct band gap at the DFT-PBE and GW methods with inclusion of SOC, respectively. $E_g^{Exp.}$ is the measured gap. E_g^{opt} is the lowest-energy absorption peak position with including the *e-h* coupling, and E_b is the binding energy of the lowest-energy bound exciton.

	E_g^{PBE}(eV)	$E_g^{PBE+SOC}$(eV)	E_g^{GW}(eV)	E_g^{GW+SOC}(eV)	E_g^{opt}(eV)	$E_g^{Exp.}$(eV)	E_b (eV)
Bulk Te	0.19	0.03	0.41	0.25	0.42	0.32–0.33 [38]	< 0.01
Monolayer Te	1.45	1.02 (1.03 [21])	2.35	1.92	1.68	0.92 [20]	0.67
Te Chain	1.75 (1.72 [31])	1.51	4.47	4.23	2.07		2.40

optical spectra based on single-particle interband transitions without including *e-h* interactions. The overall optical absorption spectrum is anisotropic. However, for the incident light polarized perpendicular to the axial direction along Te chains, the optical spectrum is isotropic due to its trigonal structure, i.e., the optical spectra of the incident light polarized along the x and y directions are isotropic. Therefore, we only present the spectra for the incident light polarized along the x direction ($E \perp z$), which is defined in Fig. 2(b). The sharpest slope of the optical absorption is located at the direct band gap around 0.41 eV. Thus, the interband transition between the lowest conduction band and the highest valance band is active for the x/y-direction polarized light. The absorption at the onset is weak owing to the small effective mass ($0.13\,m_e$) and the low density of states (DOS). The band gap of bulk Te observed in the transmission spectra and photoconductivity spectra experiments is 0.32–0.33 eV, which is slightly smaller than the calculated BSE optical gap of 0.41 eV without SOC. With SOC included, the calculated gap is estimated to decrease to 0.25 eV.

In Fig. 2(c), we present the optical absorption spectrum for the incident light polarized parallel to the axial direction of Te chains ($E//z$). Interestingly, the optical absorption starts at around 0.56 eV, which is about 140 meV higher than that in Fig. 2(b). This is because the interband transition between the lowest conduction band and the highest valance band is forbidden for the parallel-polarized incident light due to the crystal symmetry. Our simulation shows that the lowest-energy optical absorption in Fig. 2(c) starts from the transition between the second highest valance band to the lowest conduction band around the H point. The first optical absorption for the incident light polarized perpendicular to the z axis is about twice larger than that parallel to the z axis.

After including *e-h* interactions, as shown in Figs. 2(b) and 2(c), the optical absorption spectra are barely changed. Excitonic effects in bulk Te are weaker than those in the typical bulk semiconductors. For example, the optical absorption spectrum of bulk silicon is significantly changed by *e-h* interactions although its *e-h* binding energy is small [40]. In bulk Te, the first bound exciton is formed by transitions from the highest valance band to the lowest conduction band ($v_1 \rightarrow c_1$) around the H point (corresponding to the direct band gap) with the incident light polarized perpendicular to the z direction. For the incident light parallel to the z direction, the first bright exciton is formed from the highest valence-band to the first conduction band transition ($v_1 \rightarrow c_1$) along the H→A high-symmetry line near the H point. The estimated upper limit of the exciton binding energy is less than 10 meV, which is comparable to those of other bulk semiconductors [39–41]. The strong screening in bulk semiconductors usually results in a small exciton binding energy [40,42]. Particularly, the sharp band dispersions around the band edges at the H point further reduce the *e-h* interactions due to the small effective mass of electrons and holes, and low DOS. This conclusion is further confirmed by Fig. 2(d), in which the joint density of states (JDOS) and density of excitonic states (DOES) of bulk Te are plotted together. The single-particle JDOS and two-particle DOES are identical, indicating excitonic effects are nearly negligible in bulk Te.

B. Monolayer Te

Bulk Te can be grown into ultrathin layers [17,18,20]. More recently, it has been shown that monolayer Te can be fabricated by the substrate-free solution phase process and molecular-beam epitaxy on a graphene/6H-SiC(0001) substrate [17,18,20]. The ball-stick structure of monolayer Te is presented in Figs. 1(d) and 1(e). Interestingly, the distance between 1D Te chains is substantially reduced from 0.27 nm (bulk) to 0.21 nm (monolayer), implying an enhanced interchain interaction in monolayer Te. As a result, a well-defined 2D structure can be formed in orthorhombic lattices, as shown in Fig. 1(d). Our calculated in-plane lattice constants are $a = 5.60$ Å and $b = 4.20$ Å, which are in a good agreement with recent theoretical predictions and experimental measurements [20,21,31,35]. The first BZ and high-symmetry points are shown in Fig. 1(f).

The DFT-calculated band structure without SOC (black lines) of monolayer Te is presented in Fig. 3(a). A 1.2-eV indirect band gap is observed: The VBM is located at the Γ point, while the CBM is located at the X point. The direct band gap is 1.45 eV at the Γ point. After including many-electron interactions, the overall self-energy correction is roughly a rigid shift of the DFT-calculated band structures, and the quasiparticle band gap is increased to be 2.35 eV, roughly a 62% enhancement. This is similar to those of monolayer transition-metal dichalcogenides and other 2D semiconductors [8,10,43–46]. Monolayer Te has a direct band gap of 1.03 eV at the Γ point after considering SOC shown by light-blue lines in Fig. 2(a). The band gap is enlarged to be 1.92 eV with SOC included at the GW level. The observed gap of monolayer Te is 0.92 eV by *in situ* scanning tunneling microscopy [19], which is smaller than our calculated GW gap of 1.92 eV. However, it is hard to draw a conclusion for this comparison, and many factors may attribute to this inconsistency. For example, the experimental sample is on a metallic substrate while our calculated one is freestanding. The metallic substrate will substantially enhance the electronic screening and reduce

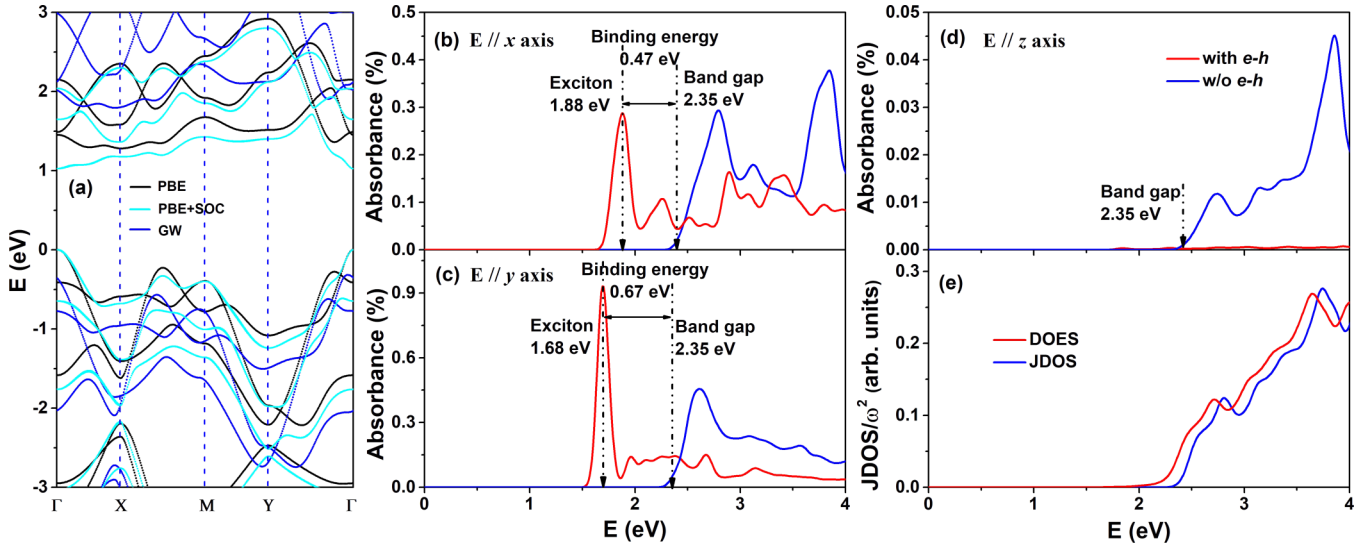

FIG. 3. (a) Band structures of monolayer Te calculated at the DFT-PBE (black line), DFT-PBE-SOC (light blue), and GW level (blue line). (b–d) Optical absorption spectra (calculated without including SOC effects) of monolayer Te for the incident light polarized along the x (b), y (c), and z (d) direction, respectively. The single-particle optical absorption spectra and those spectra with inclusion of e-h interaction are presented by the blue and the red solid line, respectively. (e) Interband JDOS (blue line) and DOES (red line) of monolayer Te (divided by ω^2 in arbitrary units).

quasiparticle band gaps [44]. Previous studies have shown that the metallic graphene substrate can reduce the quasiparticle band gap of monolayer MoS_2 by about 400 meV [47]. Moreover, the metallic substrate in experiment may introduce doping, which is another factor to reduce the quasiparticle band gap. Previous studies have shown that a moderate doping density of around $10^{13}\,cm^{-2}$ can reduce the band gap by a few hundred meV in monolayer MoS_2 [48,49]. Therefore, it is not surprising to find that our calculated quasiparticle band gap of intrinsic and freestanding monolayer Te is substantially larger than that measured in samples on metallic substrates. We expect that future experiments on suspended and intrinsic samples will reduce this discrepancy. Due to the orthorhombic geometries of the atomistic structure of monolayer Te, an anisotropic band dispersion around the band gap is observed, which is similar to that of black phosphorus [50].

Because of the artificial vacuum between monolayers in our periodic boundary condition, we cannot use the imaginary part of the dielectric function, which is not well defined in suspended 2D structures. Following Ref. [51], we define the optical absorbance, which is how much light is absorbed when the light goes through a slab structure. Because of orthorhombic in-plane lattices, the optical absorption spectrum is expected to be anisotropic, which is similar to that of monolayer black phosphorus (BP). Therefore, we plot the optical absorption spectra for the incident light polarized along the x, y, and z direction [the directions are shown in Figs. 1(d) and 1(e)] in Figs. 3(b), 3(c), and 3(d), respectively. The optical absorption spectra based on single-particle interband transitions are shown by solid blue lines, which are obviously anisotropic.

It is well known that excitonic effects are dramatically enhanced in suspended monolayer semiconductors and they dictate observed optical responses [8,42,43,46]. The optical absorption spectra with e-h interactions included are presented by the solid red line and show an obvious anisotropy. The lowest-energy bright exciton polarized along the armchair direction is located at 1.88 eV, indicating a 0.47-eV e-h binding energy [Fig. 3(b)], while the lowest-energy bright exciton polarized along the zigzag direction is located at 1.68 eV, indicating a 0.67-eV e-h binding energy [Fig. 3(c)]. These in-plane anisotropic optical absorption spectra are similar to those of monolayer BP [42,52]. As a result, we expect the photoluminescence (PL) of monolayer Te will exhibit the well-known figure-8 shaped polarization distribution just like in monolayer BP. In other words, the emission light will be dictated by the exciton located at 1.68 eV with the linear polarization along the zigzag direction.

These lowest-energy bright exciton binding energies in monolayer Te are comparable with those of monolayer graphdiyne, TMDs, and BP [8,10,12,42,46]. Our further analysis shows that the exciton at 1.68 eV polarized along the zigzag direction is mainly constructed from the band-edge states around the Γ point. The JDOS and DOES of monolayer Te are plotted in Fig. 3(e). Unlike bulk Te, the JDOS and DOES of which are nearly identical, the DOES of monolayer Te exhibits a clear redshift with respect to the JDOS due to the significant e-h attractions.

When the incident light is polarized perpendicularly to monolayer Te, another enhanced anisotropic effect is observed. As shown in Fig. 3(d), the optical absorption spectrum is completely quenched upon inclusion of e-h interactions although the single-particle interband transitions (the solid blue line) are still significant. Different from the in-plane anisotropy that is from the crystal symmetries, this anisotropy comes from a many-electron effect due to the depolarization effect or local-field effect, which is essentially from the off-diagonal elements of the nonlocal dielectric function [53]. The built-in depolarization effect from the surface boundary condition will strongly screen the external electric field of the incident

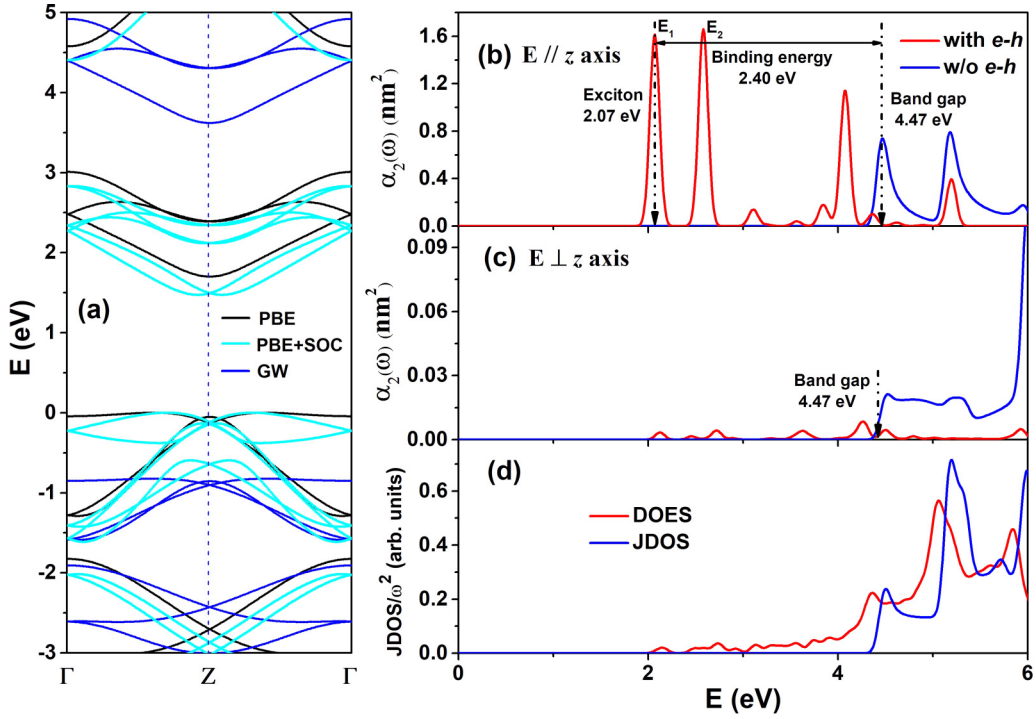

FIG. 4. (a) Band structure of chain Te. The black, light blue, and blue line represent the band structures calculated at the DFT-PBE, DFT-PBE-SOC, and GW level, respectively. (b, c) Optical absorption spectra (calculated without including SOC effects) of chain Te for the incident light polarized along (b) and vertical to (c) the chain direction. The single-particle optical absorption spectra and those spectra with inclusion of *e-h* interaction are presented by the blue and the red solid line, respectively. (d) Interband JDOS (blue line) and DOES (red line) of chain Te (divided by ω^2 in arbitrary units).

light, resulting in depressed optical absorption around the quasiparticle band gap and energy regime below it. It should be noted that the local-field effect is not an excitonic effect, because it is not due to the attractive *e-h* interaction but rather the *e-h* exchange term.

C. Chain Te

Finally, we turn to study many-electron effects and excited-state properties of the elementary building block of all the above bulk and 2D Te structures. The structure of the 1D spiral chain made by Te with the top and side views is shown in Figs. 1(g) and 1(h). Our calculated axial lattice constant is about 5.66 Å, which is similar to those of bulk and monolayer. Studies on many-electron effects of similar structures, such as 1D Se, have been reported recently [54].

The DFT-calculated and quasiparticle energy band structures of the isolated chain Te without SOC are plotted in Fig. 4(a). Similar to their bulk and 2D structures, the 1D chain of Te is an indirect semiconductor with the VBM along the $Z \rightarrow \Gamma$ direction and the CBM is located at the Γ point. The DFT-calculated indirect band gap is about 1.69 eV, and the direct band gap is 1.75 eV located at the Γ point. An enhanced self-energy correction is obtained in this 1D semiconductor: the direct band gap is increased to be 4.47 eV. This 155% enhancement of the band gap is much larger than that of bulk Te (116%) and monolayer Te (62%). It is comparable to other 1D semiconductors. For example, the self-energy corrections to the H chain, BN chain, and thin (8, 0) CNT are about 3.84, 3.93, and 1.75 eV, which are about 170, 102, and 292% of their DFT band gaps, respectively [9,55]. With SOC included, the direct band gap of a chain Te is increased to be 4.23 eV after self-energy correction.

The optical absorption spectra of 1D Te are presented in Fig. 4. As mentioned previously, the imaginary dielectric function of an isolated 1D nanostructure is not well defined. Therefore, we plot the optical absorption spectra with the imaginary part of the polarizability (α_2) per chain in units of nm^2 [56]. The calculated polarizability is defined by the dielectric susceptibility, $\chi = (\varepsilon - 1)/4\pi$, multiplied by the cross-sectional area of the supercell perpendicular to the chain axis. In Fig. 4(b), for the single-particle optical absorption spectrum, it starts from the quasiparticle band gap (~4.4 eV) and exhibits a well-defined 1D van-Hove singularity.

After including *e-h* interactions, the optical absorption spectra are completely dominated by anisotropic excitonic states. For example, we observe two bright excitons for the light polarized along the z direction, which are marked as E_1 and E_2 in Fig. 4(b). The *e-h* binding energy of the lowest-energy E_1 exciton is about 2.40 eV, which is comparable with that of the chain Se (2.77 eV) and significantly surpasses that (0.67 eV) in monolayer Te [54]. A very large exciton binding energy of 3.5 eV was calculated in the BN chain [9]. Our further analysis shows that the E_1 exciton is from the interband transitions between the first, second, and third highest valence bands and the first conduction band ($v_1, v_2, v_3 \rightarrow c_1$), while the E_2 exciton is mainly from those between the first and second highest valence bands and the second lowest conduction band ($v_1, v_2 \rightarrow c_2$) and those between the third highest valence band and the third lowest conduction band ($v_3 \rightarrow c_3$).

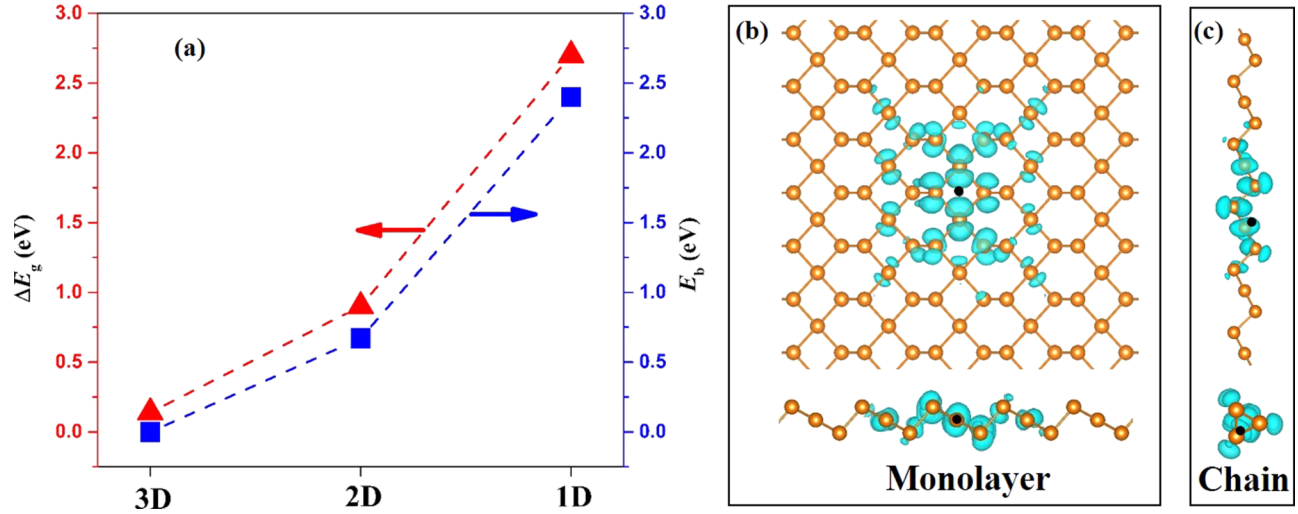

FIG. 5. (a) Evolution of the self-energy correction to the band gap and the binding energy of the first bound exciton with the dimensionality (the dashed line is a guide to the eye). (b, c) Top and side views of the first bound exciton distribution of monolayer and chain Te in real space, respectively. The hole is fixed at the black spot. The isosurface is $1 \times 10^8\, e/\mathrm{cm}^3$.

The anisotropic optical response is observed in optical absorption spectra of 1D Te. As shown in Fig. 4(c), the optical absorption for the incident light polarized perpendicularly to the axial direction of 1D Te is significantly depressed because of the similar depolarization or local-field effect, which is implemented through the *e-h* exchange interactions when solving the corresponding BSE. Finally, to further explore the optical properties of chain Te, we plot the JDOS and the DOES of chain Te. The vertical band-to-band transition starts at 4.47 eV, which corresponds to the direct quasiparticle band gap. The first absorption of the exciton is located at 2.07 eV with a small DOES.

D. Discussion

To address the dimensionality impacts on excited-state properties, we have plotted the self-energy corrections and exciton binding energies as a function of the dimensionality in Fig. 5(a) and listed these values in Table II. It is clear that many-electron effects are substantially enhanced when the dimensionality is reduced even when the materials are built by the same elementary building block, i.e., the 1D spiral Te chain. It is noteworthy that the self-energy corrections are comparable with the exciton binding energies at the same dimensionality, reflecting the similar strength of (electron-electron) *e-e* and *e-h* interactions. One reason for this enhanced quantum confinement effect is the depressed Coulomb interactions. As discussed in previous studies, the Coulomb interaction is poorly screened in suspended reduced-dimensional structures because of the vast surrounding vacuum. As a result, *e-e* and *e-h* interactions are drastically enhanced. The DFT band gap is indeed dependent on the quantum confinement that is tightly associated with dimensionality. Namely, the band gap significantly increases with the decreasing dimensionality. Actually, the DFT band gap increases from 0.19 eV in bulk Te to 1.45 eV in monolayer Te, and 1.75 eV in chain Te.

Beyond this point, we also find that the dimensionality itself and quantum confinement of wave functions also contribute significantly to enhanced many-electron effects. This is evidenced by the plot of real-space wave functions of excitons as shown in Figs. 5(b) and 5(c). Because the exciton wave function is two-body, we fix the hole at the center (marked by the black spot) and plot the corresponding electron distribution. As shown in Figs. 5(b) and 5(c), the exciton sizes in the extended direction of the 1D and 2D structures are similar, about 1 nm. This is substantially smaller than those of excitons in bulk, which are usually around tens of nm. Our estimate of the exciton size of chain Te according to the formal definition ($\langle\psi|r^2|\psi\rangle$) is smaller than that of monolayer Te. The result is consistent with the difference between *e-h* binding energies: that of 1D Te is about 2.40 eV while that of 2D Te is about 0.67 eV. The lower dimensionality always tends to enhance the *e-h* binding energy. Therefore, even with the similar exciton size in the extended direction, the dimensionality will substantially impact the *e-h* binding energy and exitonic effects in nanostructures.

Following previous work [57], the exciton binding energy is further calculated by two simple models in conjunction with the *ab initio* results. We calculate the exciton binding energy of bulk Te according to the model $E_B^{3D} = \frac{\mu}{2\varepsilon_0^2}$, where μ is the excitonic effective mass and ε_0 is the static dielectric constant. The excitonic reduced mass μ ($\frac{1}{\mu} = \frac{1}{m_e^*} + \frac{1}{m_h^*}$), where m_e^* and m_h^* are the effective mass of electron and hole, respectively, is calculated by the band structure with a value of $0.13\, m_e$, and the dielectric constant of bulk Te (28) is obtained from Ref. [58]. We get the exciton binding energy of bulk Te to be 2.2 meV, which is well consistent with the GW-BSE result that is less than 10 meV.

We also calculate the exciton binding energy of monolayer Te according to the model $E_B^{2D} = \frac{8\mu}{(1+\sqrt{1+32\pi\alpha_{2D}\mu/3})^2}$ [57], in which α_{2D} is the polarizability of monolayer Te. The polarizability α_{2D} is calculated according to the $q \to 0$ behavior of the dielectric function $\varepsilon^{-1}(q) \approx \frac{1}{1+4\pi\alpha_{2D}(1-e^{-qL/2})/L}$, in which L is the lattice constant perpendicular to the monolayer Te surface. The q point is chosen at $q = 0.001\, b_1$, where the inverse dielectric function has a value of 0.96. The excitonic reduced mass of monolayer Te is $1.49\, m_e$. The calculated

exciton binding energy of monolayer Te through this model is 0.61 eV, which is in good agreement with the GW-BSE value of 0.67 eV.

IV. CONCLUSION

In summary, first-principles many-body perturbation theory has been used to explore the quasiparticle energies and excitons evolving with the dimensionality of tellurium. Enhanced self-energy corrections to the quasiparticle band gap and *e-h* interactions are observed with the reduced dimensionality because of the depressed Coulomb screening. The binding energy of the exciton is about a few meV for bulk Te and increases to 0.67 eV for monolayer Te and even to 2.40 eV for chain Te. Strong bound excitons are formed in 2D and 1D Te with the wave function localized in the size about a few times their lattice constants. Moreover, the polarization properties with *e-h* interactions included are also dependent on the dimensionality and crystal symmetries. The optical spectra for 1D and 2D Te are anisotropic with localized excitons, while those of 3D Te are isotropic in the plane perpendicular to the direction along the spiral chain. These results shed light on the device design of Te nanostructure and disclose the connection between the dimensionality and the many-body effects.

ACKNOWLEDGMENTS

This work was supported by the National Natural Science Foundation of China (Grant No. 11674005), the National Basic Research Program of China (Grant No. 2013CB932604), and the Ministry of Science and Technology National Materials Genome Project (Grant No. 2016YFB0700601) of China. L.Y. is supported by NSF CAREER Grant No. DMR-1455346. This work used computing resources from the Extreme Science and Engineering Discovery Environment, which is supported by NSF Grant No. ACI-1548562.

[1] K. S. Novoselov, A. K. Geim, S. V. Morozov, D. Jiang, Y. Zhang, S. V. Dubonos, I. V. Grigorieva, and A. A. Firsov, Science **306**, 666 (2004).
[2] C. Berger, Z. Song, X. Li, X. Wu, N. Brown, C. Naud, D. Mayou, T. Li, J. Hass, A. N. Marchenkov, E. H. Conrad, P. N. First, and W. A. de Heer, Science **312**, 1191 (2006).
[3] A. K. Geim and I. V. Grigorieva, Nature (London) **499**, 419 (2013).
[4] A. H. Castro Neto, F. Guinea, N. M. R. Peres, K. S. Novoselov, and A. K. Geim, Rev. Mod. Phys. **81**, 109 (2009).
[5] Y. Wu, K. A. Jenkins, A. Valdes-Garcia, D. B. Farmer, Y. Zhu, A. A. Bol, C. Dimitrakopoulos, W. Zhu, F. Xia, P. Avouris, and Y. M. Lin, Nano Lett. **12**, 3062 (2012).
[6] Y. Wang, P. Huang, M. Ye, R. Quhe, Y. Pan, H. Zhang, H. Zhong, J. Shi, and J. Lu, Chem. Mater. **29**, 2191 (2017).
[7] Z. Ye, T. Cao, K. O'Brien, H. Zhu, X. Yin, Y. Wang, S. G. Louie, and X. Zhang, Nature (London) **513**, 214 (2014).
[8] G. Luo, X. Qian, H. Liu, R. Qin, J. Zhou, L. Li, Z. Gao, E. Wang, W.-N. Mei, J. Lu, Y. Li, and S. Nagase, Phys. Rev. B **84**, 075439 (2011).
[9] R. Fei, G. Luo, Y. Wang, Z. Gao, S. Nagase, D. Yu, and J. Lu, Phys. Status Solidi B **250**, 1636 (2013).
[10] H.-X. Zhong, S. Gao, J.-J. Shi, and L. Yang, Phys. Rev. B **92**, 115438 (2015).
[11] J.-H. Choi, P. Cui, H. Lan, and Z. Zhang, Phys. Rev. Lett. **115**, 066403 (2015).
[12] H. M. Hill, A. F. Rigosi, C. Roquelet, A. Chernikov, T. C. Berkelbach, D. R. Reichman, M. S. Hybertsen, L. E. Brus, and T. F. Heinz, Nano Lett. **15**, 2992 (2015).
[13] A. G. Marinopoulos, L. Reining, A. Rubio, and N. Vast, Phys. Rev. Lett. **91**, 046402 (2003).
[14] A. Coker, T. Lee, and T. P. Das, Phys. Rev. B **22**, 2968 (1980).
[15] R. Keller, W. B. Holzapfel, and H. Schulz, Phys. Rev. B **16**, 4404 (1977).
[16] B. C. Deaton and F. A. Blum, Phys. Rev. **137**, A1131 (1965).
[17] Y. Du, G. Qiu, Y. Wang, M. Si, X. Xu, W. Wu, and P. D. Ye, Nano Lett. **17**, 3965 (2017).
[18] H. O. H. Churchill, G. J. Salamo, S. Q. Yu, T. Hironaka, X. Hu, J. Stacy, and I. Shih, Nanoscale Res. Lett. **12**, 488 (2017).
[19] Y. Wang, G. Qiu, R. Wang, S. Huang, Q. Wang, Y. Liu, Y. Du, W. A. Goddard III, M. J. Kim, X. Xu, P. D. Ye, and W. Wu, Nature Electronics **1**, 228 (2018).
[20] X. Huang, J. Guan, Z. Lin, B. Liu, S. Xing, W. Wang, and J. Guo, Nano Lett. **17**, 4619 (2017).
[21] Z. Zhu, X. Cai, S. Yi, J. Chen, Y. Dai, C. Niu, Z. Guo, M. Xie, F. Liu, J. H. Cho, Y. Jia, and Z. Zhang, Phys. Rev. Lett. **119**, 106101 (2017).
[22] L. A. Agapito, N. Kioussis, W. A. Goddard III, and N. P. Ong, Phys. Rev. Lett. **110**, 176401 (2013).
[23] J. P. Perdew, K. Burke, and M. Ernzerhof, Phys. Rev. Lett. **77**, 3865 (1996).
[24] P. Giannozzi, S. Baroni, N. Bonini, M. Calandra, R. Car, C. Cavazzoni, D. Ceresoli, G. L. Chiarotti, M. Cococcioni, I. Dabo, A. Dal Corso, S. de Gironcoli, S. Fabris, G. Fratesi, R. Gebauer, U. Gerstmann, C. Gougoussis, A. Kokalj, M. Lazzeri, L. Martin-Samos, N. Marzari, F. Mauri, R. Mazzarello, S. Paolini, A. Pasquarello, L. Paulatto, C. Sbraccia, S. Scandolo, G. Sclauzero, A. P. Seitsonen, A. Smogunov, P. Umari, and R. M. Wentzcovitch, J. Phys.: Condens. Matter **21**, 395502 (2009).
[25] N. Troullier and J. L. Martins, Phys. Rev. B **43**, 1993 (1991).
[26] J. Deslippe, G. Samsonidze, D. A. Strubbe, M. Jain, M. L. Cohen, and S. G. Louie, Comput. Phys. Commun. **183**, 1269 (2012).
[27] S. Ismail-Beigi, Phys. Rev. B **73**, 233103 (2006).
[28] C. A. Rozzi, D. Varsano, A. Marini, E. K. U. Gross, and A. Rubio, Phys. Rev. B **73**, 205119 (2006).
[29] M. S. Hybertsen and S. G. Louie, Phys. Rev. B **34**, 5390 (1986).
[30] D. Y. Qiu, F. H. da Jornada, and S. G. Louie, Phys. Rev. Lett. **111**, 216805 (2013).
[31] J. Qiao, Y. Pan, F. Yang, C. Wang, Y. Chai, and W. Ji, Science Bulletin **63**, 159 (2018).
[32] J. Chen, Y. Dai, Y. Ma, X. Dai, W. Ho, and M. Xie, Nanoscale **9**, 15945 (2017).
[33] N. Bouad, L. Chapon, R. M. Marin-Ayral, F. Bouree-Vigneron, and J. C. Tedenac, J. Solid State Chem. **173**, 189 (2003).

[34] C. Adenis, V. Langer, and O. Lindqvist, Acta Cryst. **C42**, 941 (1989).
[35] Z. Zhu, X. Cai, C. Niu, C. Wang, Q. Sun, X. Han, Z. Guo, and Y. Jia, arXiv:1605.03253 (2016).
[36] L. Xian, A. Pérez Paz, E. Bianco, P. M. Ajayan, and A. Rubio, 2D Mater. **4**, 041003 (2017).
[37] R. S. Caldwell and H. Y. Fan, Phys. Rev. **114**, 664 (1959).
[38] V. B. Anzin, M. I. Eremets, Y. V. Kosichkin, and A. M. Shirokov, Phys. Status Solidi A **42**, 385 (1977).
[39] M. Rohlfing and S. G. Louie, Phys. Rev. Lett. **81**, 2312 (1998).
[40] M. Rohlfing and S. G. Louie, Phys. Rev. B **62**, 4927 (2000).
[41] M. Rohlfing and S. G. Louie, Phys. Rev. Lett. **80**, 3320 (1998).
[42] V. Tran, R. Soklaski, Y. Liang, and L. Yang, Phys. Rev. B **89**, 235319 (2014).
[43] M. Rohlfing and S. G. Louie, Phys. Rev. Lett. **83**, 856 (1999).
[44] M. M. Ugeda, A. J. Bradley, S. F. Shi, F. H. da Jornada, Y. Zhang, D. Y. Qiu, W. Ruan, S. K. Mo, Z. Hussain, Z. X. Shen, F. Wang, S. G. Louie, and M. F. Crommie, Nat. Mater. **13**, 1091 (2014).
[45] S. Huang, Y. Liang, and L. Yang, Phys. Rev. B **88**, 075441 (2013).
[46] Y. Liang, S. Huang, R. Soklaski, and L. Yang, Appl. Phys. Lett. **103**, 042106 (2013).
[47] C. Zhang, A. Johnson, C. L. Hsu, L. J. Li, and C. K. Shih, Nano Lett. **14**, 2443 (2014).
[48] S. Gao and L. Yang, Phys. Rev. B **96**, 155410 (2017).
[49] Y. Liang and L. Yang, Phys. Rev. Lett. **114**, 063001 (2015).
[50] R. Fei and L. Yang, Nano Lett. **14**, 2884 (2014).
[51] L. Yang, J. Deslippe, C.-H. Park, M. Cohen, and S. Louie, Phys. Rev. Lett. **103**, 186802 (2009).
[52] X. Wang, A. M. Jones, K. L. Seyler, V. Tran, Y. Jia, H. Zhao, H. Wang, L. Yang, X. Xu, and F. Xia, Nat. Nanotechnol. **10**, 517 (2015).
[53] C. D. Spataru, S. Ismail-Beigi, L. X. Benedict, and S. G. Louie, Appl. Phys. A **78**, 1129 (2004).
[54] E. Andharia, T. P. Kaloni, G. J. Salamo, S.-Q. Yu, H. O. H. Churchill, and S. Barraza-Lopez, Phys. Rev. B **98**, 035420 (2018).
[55] C. D. Spataru, S. Ismail-Beigi, L. X. Benedict, and S. G. Louie, Phys. Rev. Lett. **92**, 077402 (2004).
[56] C.-H. Park, C. Spataru, and S. Louie, Phys. Rev. Lett. **96**, 126105 (2006).
[57] T. Olsen, S. Latini, F. Rasmussen, and K. S. Thygesen, Phys. Rev. Lett. **116**, 056401 (2016).
[58] K. F. Young and H. P. R. Frederikse, J. Phys. Chem. Ref. Data **2**, 313 (1973).